Description of bow-tie nanoantennas excited by localized emitters using conformal transformation

Víctor Pacheco-Peña[†,ξ], Miguel Beruete[†,§], Antonio I. Fernández-Domínguez[‡], Yu Luo[χ], Miguel Navarro-Cía[*,Ω,ξ]

[†] Antennas Group – TERALAB, Universidad Pública de Navarra, 31006 Pamplona, Spain

[ξ] Optical and Semiconductor Devices Group, Imperial College London, London SW7 2AZ, UK

[§] Institute of Smart Cities, Public University of Navarra, 31006 Pamplona, Spain

[‡] Departamento de Física Teórica de la Materia Condensada and Condensed Matter Physics Center (IFIMAC), Universidad Autónoma de Madrid, Madrid 28049, Spain

[χ] The Photonics Institute and Centre for OptoElectronics and Biophotonics, School of Electrical & Electronic Engineering, Nanyang Technological University, Singapore 639798, Singapore

[Ω] School of Physics and Astronomy, University of Birmingham, Birmingham B15 2TT, UK

*m.navarro-cia@bham.ac.uk; Phone: +44(0)1214144664; Fax: +44(0)1214144644

KEYWORDS conformal transformation, bow-tie, nanoantenna, plasmonic, transformation optics

ABSTRACT The unprecedented advance experienced by nanofabrication techniques and plasmonics research over the past few years has made possible the realization of nanophotonic systems entering into the so-called strong coupling regime between localized surface plasmon (LSP) modes and quantum emitters. Unfortunately, from a theoretical point of view, the field is hindered by the lack of analytical descriptions of the electromagnetic interaction between strongly hybridized LSP modes and nanoemitters even within the Markovian approximation. This gap is tackled here by exploiting a conformal transformation where a bow-tie nanoantenna excited by a dipole is mapped into a periodic slab-dipole framework whose analytical solution is available. Solving the problem in the transformed space not only provides a straightforward analytical explanation to the original problem (validated using full-wave simulations) but also grants a deep physical insight and simple design guidelines to maximize the coupling between localized dipoles and the bow-tie LSP modes. The results presented here therefore pave the way for a full analytical description of realistic scenarios where quantum dots or dye molecules (modelled beyond a two-level system) are placed near a metallic bow-tie nanoantenna.

Antennas are well-known enabling devices for efficient transduction between electronic signals (guided waves) and radio or microwave radiation (non-guided waves).[1,2] Since their inception at the end of the 19th century, they have been intimately bound to wireless communication systems. However, this view has taken a different perspective in recent years within the field of nanophotonics.[3] Benefited from the recent advances in nanofabrication and optical characterization techniques, as well as the accuracy and predictive value that classical electromagnetics has demonstrated down to the nanoscale, the antenna concept has been revisited at optics.[4–7] The so-called nano-antennas are devices that operate in the visible range in a similar way as conventional low frequency antennas. Breaking the diffraction limit of classical

optics, these nanometric devices enable near-to-far-field coupling (and vice-versa) of optical signals with unprecedented efficiency. This nanoscale control over the propagation and confinement of visible light has already found applications in areas completely different from the traditional wireless communications such as spectroscopy,[8] biosensing,[9] photovoltaics,[10] optoelectronics,[11] photodetection[12] and nonlinear optics.[13]

Alike radio and microwave antennas, the electromagnetic response of nano-antennas is governed by their geometries and by the material properties of their components.[1] However, metals have a more complex description at visible frequencies, making the modelling and optimization of these nano-devices more challenging from a theoretical perspective. Hence, the analytical description of nano-antenna performance exists only for a few simple geometries, such as spheres, cylinders or cuboids.[14,15] Very recently, a quasi-analytical treatment of more complex nanostructures has been developed using transformation optics,[16–20] a framework similar to conformal mapping[21–24] but operating exactly at the level of Maxwell Equations.[25]

Bow-tie nano-antennas are composed by two triangular-shaped metal nanoparticles facing against each other, connected at their apexes or separated by a nanometric gap. This is one of the most thoroughly investigated structures in the literature. Experimental and numerical reports have shown the suitability of this antenna and its variations for the implementation of optical receivers and transmitters.[26–34] Compared to the other geometries examined under transformation optics such as crescents and cylindrical dimers,[20] bow-tie nano-antennas promise stronger degree of field localization and enhancement. This benefits and it is indeed essential for a myriad of plasmonic applications; for instance, the stronger the local field, the brighter the fluorescence/harmonic-signal is or the larger the Rabi splitting of molecular resonance peaks is in hybrid metal-molecule/nonlinear-material scenarios. In this work, we extend the set of nano-

antenna configurations with analytical treatment including a two-dimensional bow-tie geometry (presenting translational symmetry along one direction, as shown in Figure 1). We exploit transformation optics concepts to explain the dependence of the non-radiative decay spectra (ie., the power absorbed, P_{abs}, by the bow-tie nanoantenna under dipole illumination[20,35]) on the bow-tie geometrical parameters and to give physical insights on the coupling between oscillating classical line dipoles and the localized surface plasmon (LSP) modes supported by the bow-tie geometry.

RESULTS AND DISCUSSION

Figure 1a shows the general problem under consideration: the coupling between a line dipole (nanoemitter) with arbitrary orientation and a bow-tie nanoantenna made of silver (Ag). Notice that the tip of the bow-tie nanoantenna studied here is concave to facilitate the conformal mapping. The dipole is located on the x'-axis 1 nm away from the center of the bow-tie. This is indeed a more realistic situation than placing the dipole inside the gap, since nanometer-size gaps are in general inaccessible for nano- and micrometer-size emitters. The bow-tie is defined by the arm length, $L_1'+L_2'$, the arm angle, θ', and the gap between arms. The arm length along with the gap gives the total length of the bow-tie l'. We restrict the study to bow-tie geometries much smaller than the illumination wavelength to be within the realm of near-field (quasi-static) approximation. In this scenario, magnetic and electric fields are decoupled, and the latter can be fully described by an electrostatic potential satisfying Laplace's equation. For simplicity, the bow-tie geometries are embedded in vacuum, and the dielectric function of Ag is taken from Palik's experimental data (see the Methods section for more details of the numerical study).[36]

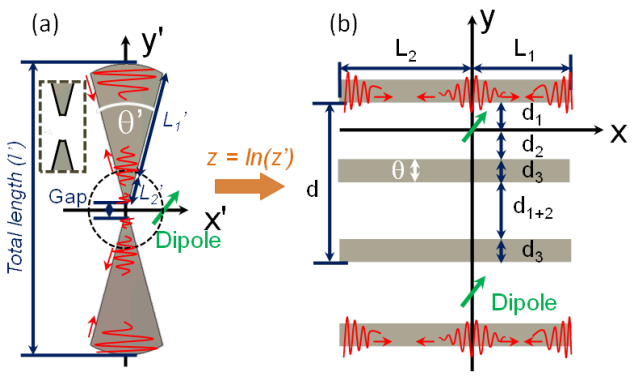


Figure 1. (a) Schematic representation of a metallic bow-tie nanoantenna with a gap on its center illuminated with a dipole placed at (x', y') = (1 nm, 0) (green arrow). (b) Transformed geometry after the conformal mapping is applied to the bow-tie nanoantenna

The system can be qualitatively explained with a simple heuristic analysis. The radiation from the localized oscillating dipole (an atom or a quantum dot in an excited state, for instance) is coupled to the different LSP modes supported by the bow-tie nanoantennas. This pumped electromagnetic energy is eventually dissipated due to metal absorption, i.e., non-radiative damping. Given the sub-wavelength size of the bow-tie, radiation loss, i.e., radiative damping, is negligible. The strength of the coupling, and thus, the non-radiative damping, depends on the position of the dipole within the field distribution of the LSP modes. In general, the problem of finding the optimum set of parameters for a specific experiment is addressed by performing brute-force computations. An alternative to reduce the computational requirements is devising analytical solutions. In the next section we derive a conformal mapping solution for the bow-tie nanoantenna excited by a dipole. We transform the problem into a geometry that can be easily solved analytically, simplifying the calculation and analysis of the original problem.

Theoretical analysis: Conformal mapping

The bow-tie can be transformed into the multi-slab geometry shown in Figure 1b by applying the following conformal transformation:

$$z = \ln(z') \tag{1}$$

where $z = x+iy$ and $z' = x'+iy'$ are the spatial coordinates in the transformed and original frame, respectively. Through this conformal transformation, circular (radial) lines in the original geometry are mapped into vertical (horizontal) lines in the transformed frame.[16,30] This transformation results in a multi-slab geometry with the dimensions of all metal slabs as L_1+L_2 and θ (= d_3) along the x-and y- axis, respectively. The original dipole is meanwhile converted into an array of dipoles with the same strength placed along the y-axis with a periodicity 2π, i.e., at ($x = 0$, $y = 2\pi m$), where m is an integer. It is worth pointing out that a scenario involving a nanoantenna with three arms would be converted into a multi-slab geometry with an additional slab per period (see Supporting Information).

By looking at the multi-slab geometry, a qualitative and quantitative (detailed next) understanding of the LSP modes supported by the bow-tie nanoantenna can be achieved. As it is shown in Figure 1b the dipole array emission triggers surface plasmons propagating along both positive and negative directions of x in the multi-slab geometry; which are mapped into the plasmonic modes excited by the single emitter along both arms of the bow-tie nanoantenna. Because of the finite length of the slab/bow-tie-arms, these surface plasmons are reflected back and forth between the two ends of the structure, forming a standing wave pattern that gives rise to the LSP modes. Hence, the continuous surface plasmon polariton spectrum of an infinite slab or bow-tie is converted into a finite set of discrete LSPs , characterized by the mode order n [37,38] (see the Methods section and Supporting Information).

The 2D conformal transformation ensures that the material properties remain unchanged, unlike the 3D counterpart.[17–20] In addition, it preserves the potential in each coordinate system:[37]

$$\phi(x,y) = \phi'(x',y') \tag{2}$$

where ϕ and ϕ' are the electrostatic potentials in the transformed and original frames, respectively. Therefore, the x' and y' components of the electric field distribution ($E'_{x'}$ and $E'_{y'}$, respectively) in the original geometry can be directly deduced from eq 2 as:[38,39]

$$E'_{x'} = -\frac{\partial \phi'}{\partial z'}\frac{\partial z}{\partial x'} - \frac{\partial \phi'}{\partial z'^{*}}\frac{\partial z'^{*}}{\partial x'} = -\frac{\partial \phi'}{\partial z'} - \frac{\partial \phi'}{\partial z'^{*}} \tag{3}$$

$$E'_{y'} = -\frac{\partial \phi'}{\partial z'}\frac{\partial z}{\partial y'} - \frac{\partial \phi'}{\partial z'^{*}}\frac{\partial z'^{*}}{\partial y'} = -i\frac{\partial \phi'}{\partial z'} + i\frac{\partial \phi'}{\partial z'^{*}} \tag{4}$$

Hence, by solving the problem in the multi-slab frame, the bow-tie scenario is solved straightforwardly. Notice that, in the multi-slab geometry, the field distribution along the y direction (E_y) actually represents the azimuthal component of the electric field ($E'_{\varphi'}$) in the bow-tie scenario, which can be calculated from the x' and y' components (eqs 3-4) as $E'_{\varphi'} = -E'_{x'}\sin(\varphi')+E'_{y'}\cos(\varphi')$, with $\varphi' = \tan^{-1}(y'/x')$. On the other hand, the field distribution along the x direction (E_x) is directly transformed into the radial component of the electric field in the original geometry ($E'_{\rho'}$), which can be obtained as $E'_{\rho'} = E'_{x'}\cos(\varphi')+E'_{y'}\sin(\varphi')$. From here on, the azimuthal and radial components will be used to represent the electric field distribution in the bow-tie nanoantennas here studied. The quantitative details of the analytical formulation to calculate the plasmonic response of the bow-tie nanoantenna is derived in the Methods section, where the problem is solved for the multi-slab geometry.

Non-radiative decay in the gap bow-tie nanoantenna

Since the energy is conserved in the transformation, the power dissipation is the same in both frames. Hence, the non-radiative decay of the nanoemitter can be deduced by calculating the power dissipated in the multi-slab geometry. This can be obtained by evaluating the electric field at the dipole position in the original frame, as follows:

$$P_{nr} = P_{abs} = -\frac{1}{2}\omega \mathrm{Im}\left\{p_x E^{s}_{1x}(x, y=0) + p_y E^{s}_{1y}(x, y=0)\right\} \tag{5}$$

where P_{nr} is the non-radiative power emission, $\omega=2\pi c/\lambda_0$ is the angular frequency at the working wavelength λ_0 and c is the velocity of light in vacuum, p_x and p_y are the components of the dipole moment along the x and y directions, and E_{1x}^s and E_{1y}^s are the components of the electric field along x and y directions in the region where the dipole is placed ($d_2 < y < d_1$). Importantly, in our calculations, an intrinsic quantum yield equal to 1 is assumed for the nanoemitter, which allows identifying the non-radiative decay experienced by the emitter and the power absorbed by the bow-tie nanoantenna.[40] Moreover, note that as eq 5 is derived in the quasi-static approximation, the expression for the extincted power by a point dipole can be used to describe the nanoemitter non-radiative decay.

Plasmonic response of gap bow-tie nanoantennas

Changing the bow-tie arm angle

Let $\Gamma_0(\omega)$ and $\Gamma_{nr}(\omega)$ be the isolated dipole radiative rate and the non-radiative decay rate for the full system. Figure 2 renders the evolution of the non-radiative Purcell enhancement rate spectra $\Gamma_{nr}(\omega)/\Gamma_0(\omega)$ (calculated as the ratio of the power absorbed by the nanoparticle P_{nr} and the total power radiated by the isolated localized emitter P_0, i.e., $\Gamma_{nr}(\omega)/\Gamma_0(\omega) = P_{nr}/P_0$)[3,20,35] as a function of θ' for a bow-tie nanoantenna with total length l'=20 nm and a normalized gap between both arms of $0.05l'$. The analytical results are evaluated using eq 5 along with the power radiated by the dipole $P_0=(1/16)(\omega^3\mu_0)(|p|^2)$ with μ_0 the permeability of vacuum and $|p|$ the magnitude of the dipole moment, respectively. The analytical results are compared with numerical calculations done with the commercial software Comsol Multiphysics (see the Methods section). The analytical results for the vertically oriented dipole case (Figure 2a) show that the maximum of $\Gamma_{nr}(\omega)/\Gamma_0(\omega)$ shifts from ~698 nm to ~394 nm when the angle θ' varies from 5º to 45º. This peak originates from the first (n = 1) LSP mode supported by the bow-tie

nanoantenna, as we show below through the field distribution inspection. Similarly, for a horizontal dipole, the first non-radiative peak due to the first LSP mode is blue-shifted from ~650 nm to ~337 nm, see Figure 2e. Although similar trends are observed in the full-wave simulations, there is an evident blue-shift between simulation results (Figure 2c,g) and analytical calculations for both dipole orientations (Figure 2a,e). The blue-shift arises from the assumption that the LSP modes acquire a phase shift of π upon reflection at each end of the metal slabs, i.e., at the open boundaries (at L_1 and $-L_2$). To account for a different reflection phase shift, a correction is introduced in the form of an extra phase $\Delta\varphi$. The calculation of $\Delta\varphi$ is done by fitting the analytically-computed wavelength of the fundamental mode (n = 1 LSP mode) to the simulations. Since higher order LSP modes may experience different reflection conditions than the fundamental one, this correction may not apply for higher order modes. The values of $\Delta\varphi$ for a vertical and horizontal dipole as a function of the angle θ' are shown in Figure 2d,h, respectively. A linear slope is obtained for angles from 5º to 15º while this tendency varies for larger angles. The corrected $\Gamma_{nr}(\omega)/\Gamma_0(\omega)$ is shown in Figure 2b,f for a vertical and horizontal dipole, respectively. Now, a good agreement between analytical and numerical results is obtained. As explained before, due to the finite size of the bow-tie nanoantennas (and the equivalent transformed problem) the LSPs are distributed as a set of discrete modes in the spectra. The resonant condition of these discrete LSP modes and their spectral distribution are provided in the Supporting Information for several bow-tie angles excited by both vertical and horizontal dipoles. From now on, $\overline{\Gamma_{nr}} = \Gamma_{nr}(\omega)/\Gamma_0(\omega)$ will refer to the corrected results.

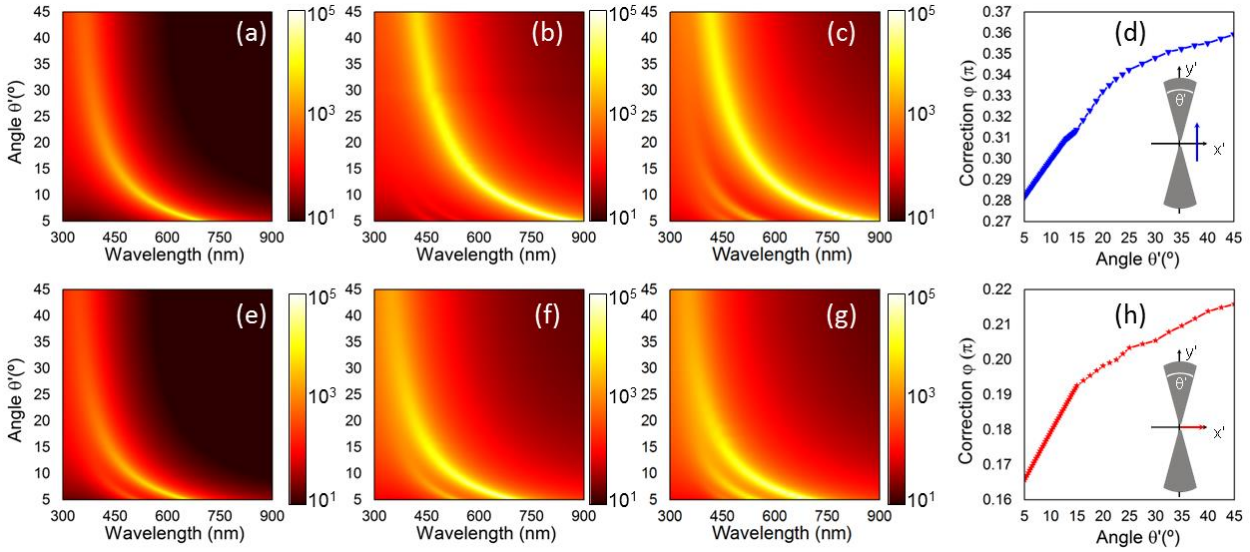


Figure 2. Non-radiative Purcell enhancement spectra as a function of the bow-tie angle θ' for a dipole with vertical (a-d) and horizontal orientation (e-h): analytical results without (a,e) and with correction (b,f) to fit simulation results (c,g). Phase correction applied in the analytical calculations for a dipole with vertical (d) and horizontal (h) polarization.

Next, we analyze in detail the analytical and simulation results of the non-radiative Purcell enhancement spectra for two bow-tie nanoantennas with θ' = 5º and 30º excited by a vertical (Figure 3a) and horizontal dipole (Figure 3b). Letting $\Gamma_r(\omega)$ be the radiative decay rate for the full system, the simulation results of the radiative Purcell enhancement $\overline{\Gamma_r} = \Gamma_r(\omega)/\Gamma_0(\omega)$ (calculated as the ratio of the power radiated by the system enclosed by the nanoparticle-dipole P_r and P_0; $\Gamma_r(\omega)/\Gamma_0(\omega) = P_r/P_0$)[3,20,35] are also shown in the same figure for completeness. Notice that it is consistently at least two orders of magnitude smaller than $\overline{\Gamma_{nr}}$, and thus negligible, as we assumed initially. A good quantitative agreement between analytical and numerical results is shown in Figure 3a,b for the first non-radiative peak while the other peaks are slightly blue-shifted, as expected from the above discussion on $\Delta\varphi$. An average blue-shift of 0.9% and 2% is

observed between the simulation and analytical results for the peak associated to the n = 2 LSP mode for the bow-tie nanoantenna with θ' = 5º for a vertical and horizontal dipole, respectively.

The simulation results of $\overline{\Gamma_{nr}}$ and $\overline{\Gamma_{r}}$ along with the absorption cross sections of the bow-tie nanoantennas under plane-wave illumination are shown in the Supporting Information.

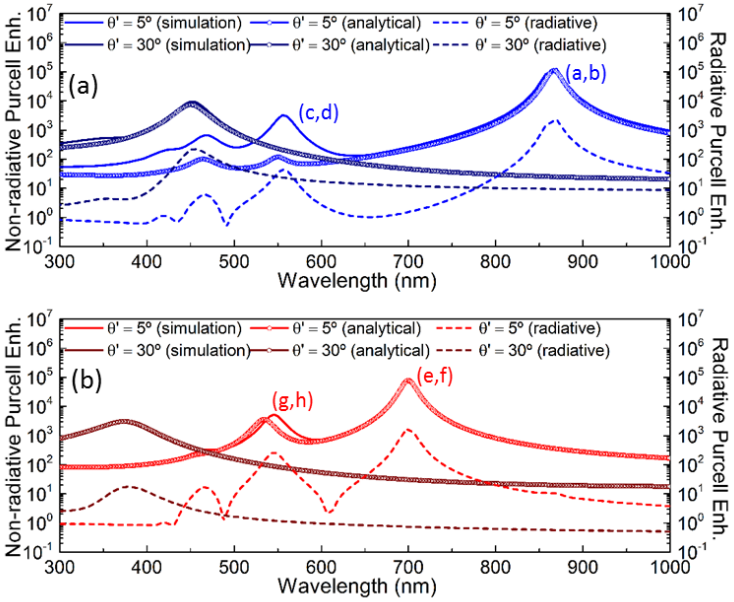


Figure 3. Analytical (dots) and simulation (solid lines) results of the non-radiative Purcell enhancement spectra along with the simulation results of the radiative Purcell enhancement spectra (dashed lines) for two bow-ties with angle θ' = 5° (light lines) and θ' = 30° (dark lines) when a vertical (a) and horizontal (b) dipole is used as a radiative source. The letters next to the peaks refer to the different panels in Figure 4.

Figure 4 shows the spatial absorption profiles across the bow-tie nanoantenna with θ' = 5° and different dipole orientation calculated at the wavelengths highlighted in Figure 3. The same results for θ' = 30° can be found in the Supporting Information. A good agreement between analytical and simulation results is noticed. As expected, when several absorption maxima exist, the absolute one is obtained closer to the apexes for all cases. This is a consequence of the larger

field concentration close to the gap which happens due to the spatial compression of the surface plasmon modes.[30] The spatial absorption distribution for the fundamental mode under a vertical dipole illumination (Figure 4a,b) has an absorption minimum pointed out by white horizontal arrows at y' = 2.2 nm (y' = 2.36 nm) in the analytical (numerical) calculation. This absorption minimum represents the node of the n = 1 LSP mode. For the peaks associated to the n = 2 LSP mode, Figure 4c,d, one can however notice a local maximum at y' = 2.06 nm (y' = 1.8 nm) in the analytical (numerical) results located at each arm of the bow-tie nanoantenna, pointed out by horizontal green arrows. This occurs because this position corresponds to the anti-node of the n = 2 LSP mode. Under horizontal dipole illumination, the positions of the maxima and minima change according to the anti-nodes of the corresponding LSP modes, as it is demonstrated next through electric field distribution patterns. Therefore, the bow-tie nanoantennas investigated here have a multi-band absorption response that arises from the efficient coupling of the localized emitter to the multiple LSP modes supported within the range from 300 nm to 900 nm.

A snapshot of the field distribution for a bow-tie nanoantenna with θ' = 5º is shown in Figure 5 for the first and second peak of $\overline{\Gamma_{nr}}$ of each dipole orientation. For convenience, here we plot $E'_{\varphi'}$ and $E'_{\rho'}$ for the vertical and horizontal dipole excitation, respectively. From these color plots we can clearly identify the mode order of the various LSPs. Under a vertical dipole illumination, the azimuthal field distribution at the first $\overline{\Gamma_{nr}}$ peak has a null between the field maxima at the edges of each bow-tie arm (Figure 5a). For the second peak (Figure 5b), we have three anti-nodes and two nulls along the radial direction in each arm, which corresponds to the n = 2 LSP mode. On the other hand, for the case of a horizontally oriented emitter, two minima appear at both ends of each arm with an anti-node between them at the lowest $\overline{\Gamma_{nr}}$ peak (Figure 5c), which corresponds to the n = 1 LSP mode. At the second peak (Figure 5d) the field distribution can be

linked to the n = 2 LSP mode as it has three nulls (one at the center and two at the extremes of each arms) and 2 maxima in between consecutive nulls. Notice that the electric field is stronger at the anti-nodes nearby the apex of the bow-ties, as expected from the spatial absorption profiles. Alternatively, the field distribution can be easily associated to standing wave patterns in the transformed frame, as it is elaborated in the Supporting Information.

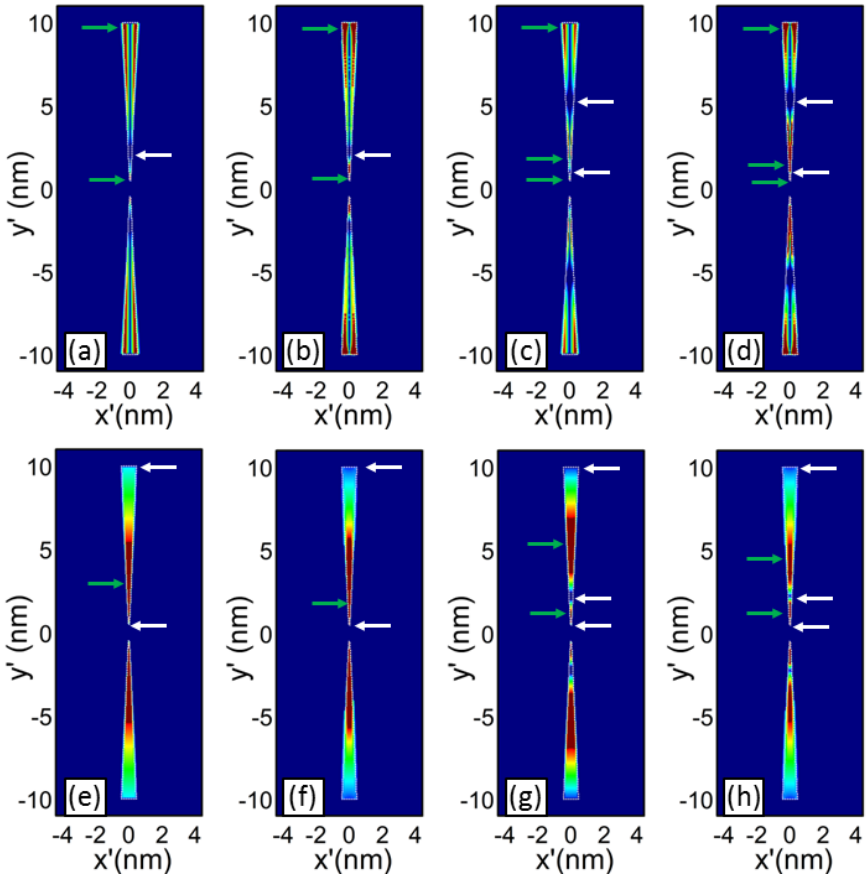


Figure 4. Analytical (a,c,e,g,) and simulation-computed (b,d,f,h) absorption for the bow-tie with angle θ' = 5° when the illuminating dipole is vertical (top) and horizontal (bottom): fundamental (a,b,e,f) and second non-radiative decay rate peak (c,d,g,h) within the spectral window of interest. The scale color bar is saturated to facilitate the intelligibility. Horizontal green and white arrows indicate respectively the location of the maxima and minima on the top arm of each bow-tie.

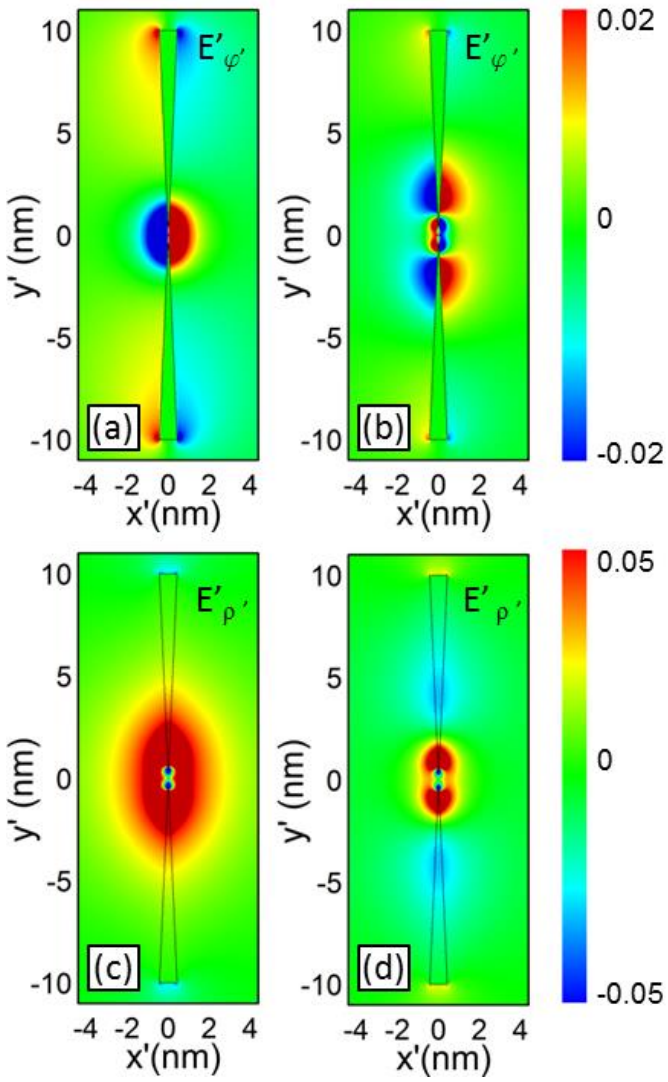


Figure 5. Snapshot of $E'_{\varphi'}$-field (top row) and $E'_{\rho'}$-field (bottom row) for a bow-tie nanoantenna with angle $\theta' = 5°$ and illuminated with a vertical (a,b) and a horizontal (c,d) dipole at the peaks in Figure 3: (a) 869 nm, (b) 556 nm, (c) 698 nm and (e) 545 nm. Note that the scale bar has been saturated from -0.02 to 0.02 and from -0.05 to 0.05 to better appreciate the field distribution across the whole space.

Changing the gap of the bow-tie nanoantenna

All the results discussed in the previous sections have been obtained considering bow-tie nanoantennas with varying θ'. We discuss next the influence of the gap size in the non-radiative

spectra of two bow-tie nanoantennas with $\theta' = 5º$, for a fixed antenna length ($l' = 20$ nm). The Supporting Information contains the results for $\theta' = 30º$. The analytical results for $\overline{\Gamma_{nr}}$ as a function of the gap distance between both arms are shown in the first row of Figure 6 when a vertical (Figure 6a) and a horizontal (Figure 6b) dipole is placed at ($x' = 1$ nm, $y' = 0$ nm). It can be observed that all peaks (related to a specific LSP mode) for both polarizations and angles are blue-shifted when the gap is increased. This blue-shift can be easily explained in terms of the transformed multi-slab geometry: an increment of the gap between both arms of the bow-tie nanoantenna is equivalent to reducing the total length of the slabs in the transformed frame (i.e., $L = L_1 + L_2$ is reduced). Hence, the resonant condition (of the standing wave pattern) happens for shorter wavelengths.

To facilitate the description and comparison, the corresponding numerical spectra are shown in the second row of Figure 6. These panels demonstrate a very good agreement with the analytical results. For $\theta' = 5º$ and a vertical dipole (Figure 6a,c) the $\overline{\Gamma_{nr}}$ peak related to the $n = 1$ LSP mode is blue-shifted from ~1132 nm (not shown) to ~845 nm when the normalized gap goes from $0.01l'$ to $0.06l'$. Interestingly, this peak is not always the $\overline{\Gamma_{nr}}$ absolute maximum, in contrast to what happens for the absorption cross section for a bow-tie under plane-wave illumination (shown in the bottom row of Figure 6). For instance, $\overline{\Gamma_{nr}}$ is larger for the $n = 2$ LSP mode for a normalized gap of $0.01l'$. This shows that there are preferred positions to increase the transfer of energy from the radiative dipole source to the different LSP modes. In particular, for the case $0.01l'$, the vertical dipole is located at a field distribution null of the $n = 1$ LSP eigen-mode (not shown here). Hence the peak associated to this mode vanishes. For the case of a horizontal dipole (Figure 6b,d) the peak due to the $n = 1$ LSP mode is blue-shifted from ~769 nm to ~697 nm when the normalized gap is increased from $0.01l'$ to $0.06l'$. The two other non-radiative peaks

(related to the n = 2 and n = 3 LSP modes, respectively) are also blue-shifted as the gap is increased. Here, the analytical $\overline{\Gamma_{nr}}$ peaks due to second and third higher order mode are also blue-shifted from simulation results by an averaged percentage of 1.1% and 1.37%, respectively, for a vertical dipole, and 1.67% and 1.2% for an horizontal dipole. The blue-shift is smaller for a horizontal dipole because of the comparatively shorter phase correction applied to this configuration.

As it has been described before, depending of the angle θ', gap, and orientation of the dipole, the localized emitter cannot transfer energy efficiently to the LSP modes (displayed as minima in the non-radiative Purcell enhancement). This phenomenon can be easily explained by looking at the multi-slab geometry. Let us then analyze the case of the bow-tie with θ' = 5º illuminated with a horizontal dipole (Figure 6b,d, analytical and simulation results, respectively). It can be observed that there is a range of gaps between ~0.028l' to ~0.038l' where the peak linked to the n = 3 LSP mode vanishes. To investigate in detail this feature, the $\overline{\Gamma_{nr}}$ for this bow-tie nanoantenna using a horizontal dipole is shown in Figure 7a,e for a normalized gap of 0.057l' and 0.035l', respectively (these panels have been extracted from the black dashed lines of Figure 6b). For the case of a gap of 0.057l', Figure 7a shows that three peaks are present at ~691 nm, ~522 nm and ~454 nm which are those related to the LSP modes with n = 1, 2 and 3, respectively. On the other hand, when the gap is 0.035l' (Figure 7e) all peaks are red-shifted, as expected, to ~721 nm, ~556 nm and ~433 nm. Nevertheless, the LSP mode with n = 3 at ~433 nm almost disappears.

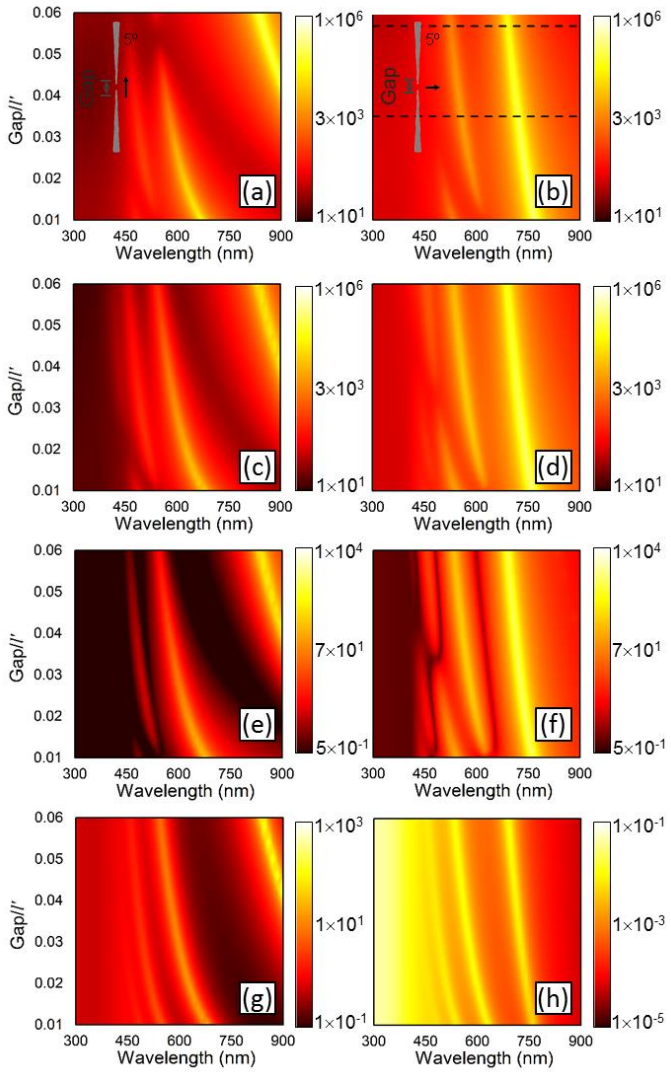


Figure 6. Analytical (first row) and simulated (second row) non-radiative Purcell enhancement spectra along with the simulation results of the radiative Purcell enhancement spectra (third row) and absorption cross section (fourth row) as a function of the gap between the arms for the bow-tie with angle $\theta' = 5°$ when a vertically (first column) and horizontally (second column) polarized dipole (top three rows) or plane-wave is used as a source (bottom row).

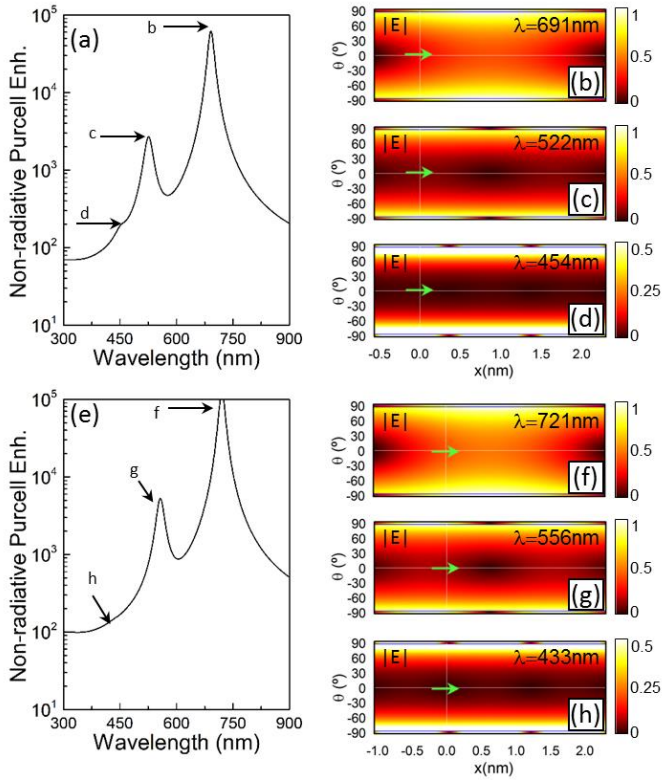


Figure 7. Analytical non-radiative Purcell enhancement spectra for a bow-tie with θ'= 5° and gap = 0.057*l'* (a) and 0.035*l'* (e). Analytical normalized magnitude of the electric field for the parallel-plate geometry at the relevant spectral position shown in (a) and (e). The position of the illuminating horizontal dipole is shown as a green arrow for aid. Note that the scale in (d) and (h) has been saturated from 0-0.5 to better observe the field distribution

This phenomenon can be explained by analyzing the fields in the transformed geometry, as follows: first, the analytical results of the normalized magnitude of the electric field distribution in the multi-slab geometry for the case of a gap of 0.057*l'* at the first, second and third peaks is shown in Figure 7b-d, respectively. The field distribution at these peaks corresponds to the field distribution of the LSP modes with n = 1, 2 and 3, respectively, as it has been explained before. For the case of the first LSP mode (n = 1) the horizontal dipole (schematically shown as an

horizontal green arrow) is placed close but not just at the node at $-L_2$ (i.e., the node in the standing wave pattern) of the field distribution; therefore, the dipole can couple to this LSP mode. However, for $n = 2$ (Figure 7c) the dipole is closer to the first node, where poorer transfer of energy between the dipole to the LSP is expected. Hence, a reduction of $\overline{\Gamma_{nr}}$ takes place for this mode compared to the first one. Similar performance can be observed for $n = 3$. In this case, the dipole is even closer to the node compared with the first and second modes; therefore, the amplitude of the peak is reduced although it still appears in the spectrum. Now, let us analyze the case when the gap is 0.035*l'*. For this geometry, the normalized magnitude of the electric field at 721, 556 and 433 nm is shown in Figure 7f-h, respectively. As it can be observed in Figure 7h, the field distribution corresponds to the LSP mode with $n = 3$, as explained before. Moreover, it is shown that the horizontal dipole is exactly at the position where the distribution of the electric field has a node. Therefore, the electromagnetic energy released by the dipole does not couple efficiently to this LSP mode giving rise to a null in $\overline{\Gamma_{nr}}$. On the contrary, for the case of the first and second peaks (see Figure 7f,g, respectively) the horizontal dipole is located at a more favorable position for energy transfer to the LSP modes than for the $n = 3$ LSP mode and the $n =$ 1 and 2 LSP modes for 0.057*l'* gap; Hence, the non-radiative decay rate is higher for them.

CONCLUSIONS

In conclusion, an analytical solution for bow-tie nanoantennas based on conformal transformation in the quasi-static approximation has been rigorously derived. For situations beyond the quasi-static limit, one could explore the implementation of a radiative correction based on a fictitious absorbing dipole in the transformed space.[20,38] The conformal transformation permits to convert the original problem of a bow-tie nanoantenna excited by a local dipole into a multi-slab geometry with an array of dipoles whose solution can be found

analytically, and is also solution of the original bow-tie nanoantenna scenario. Our conformal mapping approach also enables us to describe in detail all the spectral features in the non-radiative Purcell enhancement of a nanoemitter placed in the vicinity of different bow-tie nanoantennas. These results should ease the design of bow-tie nanoantennas for multiple applications. In particular, it may hold promise to model analytically the dynamics of realistic strong coupling scenarios where localized surface plasmon modes interact with states linked to few-level emitters such as quantum dots or dye molecules.

METHODS

Multi-slab geometry mimicking the gap bow-tie nanoantenna

Here, the multi-slab geometry shown in Figure 1(b) is solved. Taking into account that the dimensions of the bow-tie nanoantenna are sufficiently smaller than the operational wavelength ($l' << \lambda_0$), the near-field approximation can be used and thus, the electric field can be fully described by an electrostatic potential satisfying Laplace's equation. As it is known, in the multi-slab geometry shown in Figure 1(b), it is possible to excite surface plasmon modes in both transversal and longitudinal directions, with their propagation along the *x*- and *y*- axis, respectively. However, the interest here is focused in the derivation of the surface plasmon modes excited in the multi-slab geometry when $L_1 + L_2 >> \theta$; thereby, the contribution of the longitudinal LSP modes (i.e., those with phase variation along *y*) can be neglected and assume that the excited LSP modes are mainly due to the transversal modes (i.e., those with phase variation along *x*). Based on this, the electrostatic potentials outside and inside the metal strips in Figure 1(b) can be calculated as a sum of all discrete transverse modes, as follows:

$$\sum_k \left[\frac{1}{1-e^{2ik(L_1+L_2)+2i\Delta\varphi}} \left(e^{ikx} + e^{-ikx+2ikL_1+i\Delta\varphi}\right)\left(A_+ e^{-ky} + B_+ e^{-ky} + B_e^{ky}\right) \right], 0 < y < d_1 \quad (6)$$

$$\sum_k \left[\frac{1}{1-e^{2ik(L_1+L_2)+2i\Delta\varphi}} \left(e^{ikx} + e^{-ikx+2ikL_1+i\Delta\varphi}\right)\left(A_e^{ky} + B_+ e^{-ky} + B_e^{ky}\right)\right], -d_2 < y < 0 \quad (7)$$

$$\sum_k \left[\frac{1}{1-e^{2ik(L_1+L_2)+2i\Delta\varphi}} \left(e^{ikx} + e^{-ikx+2ikL_1+i\Delta\varphi}\right)\left(E_+ e^{-ky} + E_e^{ky}\right)\right], -(d_1 + 2d_2 + d_3) < y < -(d_2 + d_3) \quad (8)$$

$$\sum_k \left[\frac{1}{1-e^{2ik(L_1+L_2)+2i\Delta\varphi}} \left(e^{ikx} + e^{-ikx+2ikL_1+i\Delta\varphi}\right)\left(C_+ e^{-ky} + C_e^{ky}\right)\right], -(d_1 + 2d_2 + 2d_3) < y < -(d_1 + 2d_2 + d_3) \quad (9)$$

$$\sum_k \left[\frac{1}{1-e^{2ik(L_1+L_2)+2i\Delta\varphi}} \left(e^{ikx} + e^{-ikx+2ikL_1+i\Delta\varphi}\right)\left(D_+ e^{-ky} + D_e^{ky}\right)\right], -(d_2 + d_3) < y < -d_2 \quad (10)$$

Where k is the wave vector of the transverse LSP modes calculated as $k=(n\pi-\Delta\varphi)/(L_1+L_2)$ with n = 1, 2, 3,… representing the discrete transverse SP mode, $\Delta\varphi$ is the correction of phase applied to the bow-tie nanoantenna to take into account the complex reflection experienced by the surface plasmon waves at the extremes of the nanoparticle, A_+ and A_- are the expansion coefficients of the incident potential, B_+ and B_- are the coefficients related to the scattering potential in the region where the dipole is placed ($d_2 < y < d_1$), E_+ and E_- are the coefficients of associated to the scattering potential in the region where a dipole is absent ($d_2 + d_1$) and C_+, C_-, D_+ and D_- are those corresponding to the potential inside the metal strips (d_3). The coefficients associated with the incident potential can be obtained by expanding the dipole potential along the x direction using a Fourier transform:

$$A\pm = \frac{\pm p_y - ip_x \,\mathrm{sgn}(k)}{2\varepsilon_0} \quad (11)$$

where p_y and p_x are the components of the dipole moment along the x and y directions, respectively, and ε_0 is the permittivity in vacuum.

The other eight unknown coefficients B_+, B_-, C_+, C_-, D_+, D_-, E_+ and E_- can be solved by using the boundary conditions at each interface of Figure 1(b). First, the condition of conservation of the parallel component of the electric field at the boundaries d_2, d_2+d_3, d_1 and $d_1+2d_2+2d_3$ is applied, as follows:

$$A_-e^{-kd_2} + B_+e^{kd_2} + B_-e^{-kd_2} = D_-e^{-kd_2} + D_+e^{kd_2} \tag{12}$$

$$E_+e^{k(d_2+d_3)} + E_-e^{-k(d_2+d_3)} = D_-e^{-k(d_2+d_3)} + D_+e^{k(d_2+d_3)} \tag{13}$$

$$A_+e^{-kd_1} + B_+e^{-kd_1} + B_-e^{kd_1} = C_-e^{-k(d_1+2d_2+2d_3)} + C_+e^{k(d_1+2d_2+2d_3)} \tag{14}$$

$$E_+e^{k(d_1+2d_2+d_3)} + E_-e^{-k(d_1+2d_2+d_3)} = C_-e^{-k(d_1+2d_2+d_3)} + C_+e^{k(d_1+2d_2+d_3)} \tag{15}$$

Also, the condition of conservation of the normal component of the displacement field at the same boundaries as eqs 12-15 is applied, as follow:

$$A_-e^{-kd_2} - B_+e^{kd_2} + B_-e^{-kd_2} = \varepsilon D_-e^{-kd_2} - \varepsilon D_+e^{kd_2} \tag{16}$$

$$E_+e^{k(d_2+d_3)} - E_-e^{-k(d_2+d_3)} = -\varepsilon D_-e^{-k(d_2+d_3)} + \varepsilon D_+e^{k(d_2+d_3)} \tag{17}$$

$$A_+e^{-kd_1} + B_+e^{-kd_1} - B_-e^{kd_1} = -\varepsilon C_-e^{-k(d_1+2d_2+2d_3)} + \varepsilon C_+e^{k(d_1+2d_2+2d_3)} \tag{18}$$

$$-E_+e^{k(d_1+2d_2+d_3)} + E_-e^{-k(d_1+2d_2+d_3)} = \varepsilon C_-e^{-k(d_1+2d_2+d_3)} - \varepsilon C_+e^{k(d_1+2d_2+d_3)} \tag{19}$$

where ε is the permittivity of the metal used in the structure (Silver in this case). The solutions of the potentials in the real space for the region where there is ($d_2 < y < d_1$) and there is not a dipole ($d_2 + d_1$), ϕ_1^s and ϕ_2^s, respectively, can be then obtained by applying an inverse Fourier transform to the induced potentials:

$$\phi_1^s = \frac{1}{2\varepsilon_0(L_1+L_2)}\sum_n \left\langle \Theta\left\{p_x\left[\sin(kx)-\sin(kx-2kL_1-\Delta\varphi)\right]+p_y\left[\cos(kx)+\cos(kx-2kL_1-\Delta\varphi)\right]\right\}\left(B_+e^{-ky}+B_-e^{ky}\right)\right\rangle \quad (20)$$

$$\phi_2^s = \frac{1}{2\varepsilon_0(L_1+L_2)}\sum_n \left\langle \Theta\left\{p_x\left[\sin(kx)-\sin(kx-2kL_1-\Delta\varphi)\right]+p_y\left[\cos(kx)+\cos(kx-2kL_1-\Delta\varphi)\right]\right\}\left(E_+e^{-ky}+E_-e^{ky}\right)\right\rangle \quad (21)$$

Similarly, the potentials inside both metallic slabs (ϕ_1^m and ϕ_2^m) are:

$$\phi_1^m = \frac{1}{2\varepsilon_0(L_1+L_2)}\sum_n \left\langle \Theta\left\{p_x\left[\sin(kx)-\sin(kx-2kL_1-\Delta\varphi)\right]+p_y\left[\cos(kx)+\cos(kx-2kL_1-\Delta\varphi)\right]\right\}\left(C_+e^{-ky}+C_-e^{ky}\right)\right\rangle \quad (22)$$

$$\phi_2^m = \frac{1}{2\varepsilon_0(L_1+L_2)}\sum_n \left\langle \Theta\left\{p_x\left[\sin(kx)-\sin(kx-2kL_1-\Delta\varphi)\right]+p_y\left[\cos(kx)+\cos(kx-2kL_1-\Delta\varphi)\right]\right\}\left(D_+e^{-ky}+D_-e^{ky}\right)\right\rangle \quad (23)$$

where Θ is defined as:

$$\Theta = \frac{1}{\left\{1-\cos\left[2k(L_1+L_2)+2\Delta\varphi\right]-\sin\left[2k(L_1+L_2)+2\Delta\varphi\right]\right\}} \quad (24)$$

Finally, the x and y components of the electric field can be calculated by simply differentiating the potentials:

$$E_{1x}^s = \sum_n -\frac{k}{2\varepsilon_0(L_1+L_2)}\left\langle \left\{p_x\left[\cos(kx)-\cos(kx-2kL_1-\Delta\varphi)\right]-p_y\left[\sin(kx)+\sin(kx-2kL_1-\Delta\varphi)\right]\right\}\left(B_+e^{-ky}+B_-e^{ky}\right)\right\rangle \quad (25)$$

$$E_{2x}^s = \sum_n -\frac{k}{2\varepsilon_0(L_1+L_2)}\left\langle \left\{p_x\left[\cos(kx)-\cos(kx-2kL_1-\Delta\varphi)\right]-p_y\left[\sin(kx)+\sin(kx-2kL_1-\Delta\varphi)\right]\right\}\left(E_+e^{-ky}+E_-e^{ky}\right)\right\rangle \quad (26)$$

$$E_{1x}^m = \sum_n -\frac{k}{2\varepsilon_0(L_1+L_2)}\left\langle \left\{p_x\left[\cos(kx)-\cos(kx-2kL_1-\Delta\varphi)\right]-p_y\left[\sin(kx)+\sin(kx-2kL_1-\Delta\varphi)\right]\right\}\left(C_+e^{-ky}+C_-e^{ky}\right)\right\rangle \quad (27)$$

$$E_{2x}^m = \sum_n -\frac{k}{2\varepsilon_0(L_1+L_2)}\left\langle \left\{p_x\left[\cos(kx)-\cos(kx-2kL_1-\Delta\varphi)\right]-p_y\left[\sin(kx)+\sin(kx-2kL_1-\Delta\varphi)\right]\right\}\left(D_+e^{-ky}+D_-e^{ky}\right)\right\rangle \quad (28)$$

$$E_{1y}^s = \sum_n -\frac{k}{2\varepsilon_0(L_1+L_2)}\left\langle \left\{p_x\left[\sin(kx)-\sin(kx-2kL_1-\Delta\varphi)\right]+p_y\left[\cos(kx)+\cos(kx-2kL_1-\Delta\varphi)\right]\right\}\left(-B_+e^{-ky}+B_-e^{ky}\right)\right\rangle \quad (29)$$

$$E_{2y}^{s}=\sum_{n}-\frac{k}{2\varepsilon_0(L_1+L_2)}\left\langle\left\{p_x\left[\sin(kx)-\sin(kx-2kL_1-\Delta\varphi)\right]+p_y\left[\cos(kx)+\cos(kx-2kL_1-\Delta\varphi)\right]\right\}\left(-E_{+}e^{-ky}+E_{-}e^{ky}\right)\right\rangle \quad (30)$$

$$E_{1y}^{m}=\sum_{n}-\frac{k}{2\varepsilon_0(L_1+L_2)}\left\langle\left\{p_x\left[\sin(kx)-\sin(kx-2kL_1-\Delta\varphi)\right]+p_y\left[\cos(kx)+\cos(kx-2kL_1-\Delta\varphi)\right]\right\}\left(-C_{+}e^{-ky}+C_{-}e^{ky}\right)\right\rangle \quad (31)$$

$$E_{2y}^{m}=\sum_{n}-\frac{k}{2\varepsilon_0(L_1+L_2)}\left\langle\left\{p_x\left[\sin(kx)-\sin(kx-2kL_1-\Delta\varphi)\right]+p_y\left[\cos(kx)+\cos(kx-2kL_1-\Delta\varphi)\right]\right\}\left(-D_{+}e^{-ky}+D_{-}e^{ky}\right)\right\rangle \quad (32)$$

The complete solution for each constant is not shown here due to their complexity; therefore the coefficients are used in order to reduce the equations of potentials and electric field. However, these solutions can be directly obtained either manually or using a mathematic software.

A similar mathematical derivation can be applied for a bow-tie nanoantenna composed of three arms. The corresponding results can be found in Supporting Information.

Numerical simulations

The numerical results are calculated using the commercial Finite Element Analysis software Comsol Multiphysics®. The model of metal used in this work is Silver (Ag) modeled as a Drude-Lorentz function with the form $\varepsilon_r = \varepsilon_\infty-(\omega_p^2/\omega(\omega-i\gamma))+(\varepsilon_l\omega_l^2)/(\omega_l^2-\omega^2+2i\gamma_l\omega)$; with $\varepsilon_\infty = 1.174$, Drude plasma frequency $\omega_p = 13.6973\times10^{15}$ rad/s, Lorentz plasma frequency $\omega_l = 7.5398\times10^{15}$ rad/s, $\varepsilon_l = 1.69$, Drude damping constant $\gamma = 30.58\times10^{12}$ rad/s and Lorentz damping constant $\gamma_l = 1839\times10^{12}$ rad/s. This function fits Palik's experimental data.[36] The bow tie antennas, with a total length of *l'* = 20 nm are immersed in a vacuum modeled as a two-dimensional square of 600 nm × 600 nm. In order to reduce undesirable reflections from the system, scattering boundary conditions (i.e., perfectly matched layers) have been applied to the boundaries of the square of vacuum. The 2D TM point dipole used to illuminate the nanoantenna is modeled using two anti-

parallel in-plane magnetic currents with a separation of 5 pm. Also, an extremely refined mesh has been used with a maximum and minimum mesh size of 2 nm and 3 pm, respectively for the box of vacuum. For the bow-tie nanoantennas, a refined mesh twice smaller than the mesh used for the box of vacuum is applied to ensure accurate results. For the systematic study shown in Figure 2c,g, the non-radiative power was evaluated by simulating in a frequency range from 300 THz to 1000 THz with a step of 20 THz for the following range of angles of aperture of the antennas: from 5º to 15º with a step of 0.25º and from 15º to 25º with a step of 0.5º and from 25º to 45º with a step of 1º. This parametrical study was applied for both, vertically and horizontally polarized dipole. With these parameters, the estimated time to solve each simulation (i.e. for one angle of aperture of the antennas with one polarization) was in mean 90 minutes each.

ASSOCIATED CONTENT

Supporting Information. Resonant condition and discrete distribution of the LSP modes as a function of the angle θ' for both polarizations of the localized emitter is shown in Figure S1a. The cut-off wavelength of the first 15 LSP modes for the bow-tie nanoantennas with an angle (θ') of 5º, 25º and 45º when a vertical and a horizontal dipole illuminates the bow-tie nanoantennas is shown in Figure S1b,c, respectively. Numerical results of the non-radiative and radiative enhancements along with the absorption cross section for two bow-tie nanoantennas with $\theta' = 5º$ and $\theta' = 30º$ for both polarizations are shown in Figure S2. Figure S3 illustrates the spatial absorption distribution for the bow-tie with $\theta' = 30º$. Description of the standing wave pattern in the transformed frame to support the reasoning revolving around Figure 5. The non-radiative and radiative Purcell enhancement spectra along with the absorption cross section spectra for the bow-tie with $\theta' = 30º$ and different polarization illumination are depicted in

Figure S4. The scenario comprising a line dipole (nanoemitter) with arbitrary orientation and a tripod nanoantenna made of silver along with the associated results for $\theta' = 30º$ are reported in Figure S5. "This material is available free of charge via the Internet at http://pubs.acs.org."

AUTHOR INFORMATION

Corresponding Author

* School of Physics and Astronomy, University of Birmingham, Birmingham B15 2TT, UK. m.navarro-cia@bham.ac.uk; Phone: +44(0)1214144664; Fax: +44(0)1214144644

ACKNOWLEDGMENT

The authors would like to thank Prof. Sir J. Pendry for fruitful discussions. This work was supported in part by the Spanish Government under Contract TEC2014-51902-C2-2-R. V.P.-P. is sponsored by Spanish Ministerio de Educación, Cultura y Deporte under grant FPU AP-2012-3796. M.B. is sponsored by the Spanish Government via RYC-2011-08221. Y. L. would like to acknowledge the funding support from NTU-A*STAR Silicon Technologies Centre of Excellence under the program grant No. 11235150003. M.N.-C. was supported by an Imperial College Junior Research Fellowship and is now supported by a Birmingham Fellowship.

ABBREVIATIONS

LSP, Localized Surface Plasmon

REFERENCES

(1) Balanis, C. A. *Antenna Theory: Analysis and Design*; Third Edit.; John Wiley & Sons: Hoboken, New Jersey, 2005.

(2) Pozar, D. M. *Microwave Engineering*; John Wiley & Sons: New York, 1998.

(3) Novotny, L.; Hecht, B. *Principles of Nano-Optics*; Second Edi.; Cambridge University Press: U.K., 2012.

(4) Alù, A.; Engheta, N. Input Impedance, Nanocircuit Loading, and Radiation Tuning of Optical Nanoantennas. *Phys. Rev. Lett.* **2008**, *101*, 1–4.

(5) Bharadwaj, P.; Deutsch, B.; Novotny, L. Optical Antennas. *Adv. Opt. Photonics* **2009**, *1*, 438.

(6) Alu, A.; Engheta, N. Theory, Modeling and Features of Optical Nanoantennas. *IEEE Trans. Antennas Propag.* **2013**, *61*, 1508–1517.

(7) Eggleston, M. S.; Messer, K.; Zhang, L.; Yablonovitch, E.; Wu, M. C. Optical Antenna Enhanced Spontaneous Emission. *Proc. Natl. Acad. Sci.* **2015**, *112*, 1704–1709.

(8) Giannini, V.; Fernández-Domínguez, A. I.; Heck, S. C.; Maier, S. A. Plasmonic Nanoantennas: Fundamentals and Their Use in Controlling the Radiative Properties of Nanoemitters. *Chem. Rev.* **2011**, *111*, 3888–3912.

(9) Nie, S. Probing Single Molecules and Single Nanoparticles by Surface-Enhanced Raman Scattering. *Science* **1997**, *275*, 1102–1106.

(10) Anker, J. N.; Hall, W. P.; Lyandres, O.; Shah, N. C.; Zhao, J.; Van Duyne, R. P. Biosensing with Plasmonic Nanosensors. *Nat. Mater.* **2008**, *7*, 442–453.

(11) Atwater, H. A.; Polman, A. Plasmonics for Improved Photovoltaic Devices. *Nat. Mater.* **2010**, *9*, 205–213.

(12) Knight, M. W.; Sobhani, H.; Nordlander, P.; Halas, N. J. Photodetection with Active Optical Antennas. *Science* **2011**, *332*, 702–704.

(13) Aouani, H.; Rahmani, M.; Navarro-Cia, M.; Maier, S. A. Third-Harmonic-Upconversion Enhancement from a Single Semiconductor Nanoparticle Coupled to a Plasmonic Antenna. *Nat. Nanotechnol.* **2014**, *9*, 290–294.

(14) Bohren, C. F.; Huffman, D. R. *Absorption and Scattering of Light by Small Particles*; Wiley-VCH Verlag GmbH: Weinheim, Germany, 2007.

(15) Massa, E.; Maier, S. A.; Giannini, V. An Analytical Approach to Light Scattering from Small Cubic and Rectangular Cuboidal Nanoantennas. *New J. Phys.* **2013**, *15*, 063013.

(16) Luo, Y.; Pendry, J. B.; Aubry, A. Surface Plasmons and Singularities. *Nano Lett.* **2010**, *10*, 4186–4191.

(17) Pendry, J. B.; Aubry, A.; Smith, D. R.; Maier, S. A. Transformation Optics and Subwavelength Control of Light. *Science* **2012**, *337*, 549–552.

(18) Fernández-Domínguez, A. I.; Luo, Y.; Wiener, A.; Pendry, J. B.; Maier, S. A. Theory of Three-Dimensional Nanocrescent Light Harvesters. *Nano Lett.* **2012**, *12*, 5946–5953.

(19) Pendry, J. B.; Fernández-Domínguez, A. I.; Luo, Y.; Zhao, R. Capturing Photons with Transformation Optics. *Nat. Phys.* **2013**, *9*, 518–522.

(20) Aubry, A.; Pendry, J. B. Transformation Optics for Plasmonics. In *Active Plasmonics and Tunable Plasmonic Metamaterials*; Zayats, A., Maier, S. A., Eds.; John Wiley & Sons: Hoboken, New Jersey, 2013; pp 105–152.

(21) DuHamel, R.; Isbell, D. Broadband Logarithmically Periodic Antenna Structures. *IRE Int. Conv. Rec.* **1957**, *5*, 119–128.

(22) Carrel, R. The Characteristic Impedance of Two Infinite Cones of Arbitrary Cross

Section. *IRE Trans. Antennas Propag.* **1958**, *6*, 243–245.

(23) Ramo, S.; Whinnery, J. R.; Duzer, T. Van. *Fields and Waves in Communication Electronics*; Third Edit.; John Wiley & Sons: U.K., 1965.

(24) Heiblum, M.; Harris, J. H. Analysis of Curved Optical Waveguides by Conformal Transformation. *IEEE J. Quant. Electron.* **1975**, *11*, 75–83.

(25) Xu, L.; Chen, H. Conformal Transformation Optics. *Nat. Photonics* **2014**, *9*, 1–8.

(26) Yu, N.; Cubukcu, E.; Diehl, L.; Bour, D.; Corzine, S.; Zhu, J.; Höfler, G.; Crozier, K. B.; Capasso, F. Bowtie Plasmonic Quantum Cascade Laser Antenna. *Opt. Express* **2007**, *15*, 13272–13281.

(27) Kinkhabwala, A.; Yu, Z.; Fan, S.; Avlasevich, Y.; Mullen, K.; E., M. Large Single-Molecule Fluorescence Enhancements Produced by a Bowtie Nanoantenna. *Nat. Photonics* **2009**, *3*, 654–657.

(28) Hatab, N. A.; Hsueh, C. H.; Gaddis, A. L.; Retterer, S. T.; Li, J. H.; Eres, G.; Zhang, Z.; Gu, B. Free-Standing Optical Gold Bowtie Nanoantenna with Variable Gap Size for Enhanced Raman Spectroscopy. *Nano Lett.* **2010**, *10*, 4952–4955.

(29) Ko, K. D.; Kumar, A.; Fung, K. H.; Ambekar, R.; Liu, G. L.; Fang, N. X.; Toussaint, K. C. Nonlinear Optical Response from Arrays of Au Bowtie Nanoantennas. *Nano Lett.* **2011**, *11*, 61–65.

(30) Navarro-Cia, M.; Maier, S. A. Broad-Band near-Infrared Plasmonic Nanoantennas for Higher Harmonic Generation. *ACS Nano* **2012**, *6*, 3537–3544.

(31) Aouani, H.; Navarro-Cia, M.; Rahmani, M.; Sidiropoulos, T. P. H.; Hong, M.; Oulton, R. F.; Maier, S. A. Multiresonant Broadband Optical Antennas As Efficient Tunable Nanosources of Second Harmonic Light. *Nano Lett.* **2012**, *12*, 4997–5002.

(32) Sivis, M.; Duwe, M.; Abel, B.; Ropers, C. Extreme-Ultraviolet Light Generation in Plasmonic Nanostructures. *Nat. Phys.* **2013**, *9*, 304–309.

(33) Roxworthy, B. J.; Bhuiya, A. M.; Yu, X.; Chow, E. K. C.; Toussaint, K. C. Reconfigurable Nanoantennas Using Electron-Beam Manipulation. *Nat. Commun.* **2014**, *5*, 4427.

(34) Hentschel, M.; Metzger, B.; Knabe, B.; Buse, K.; Giessen, H. Linear and Nonlinear Optical Properties of Hybrid Metallic – Dielectric Plasmonic Nanoantennas. **2016**, *7*, 111–120.

(35) Liu, M.; Lee, T.; Gray, S. K.; Guyot-sionnest, P.; Pelton, M. Excitation of Dark Plasmons in Metal Nanoparticles by a Localized Emitter. *Phys. Rev. Lett.* **2009**, *102*, 107401–1 – 4.

(36) Palik, E. D. *Handbook of Optical Constants of Solids*; Academic, 1985.

(37) Luo, Y.; Lei, D. Y.; Maier, S. A.; Pendry, J. B. Transformation-Optics Description of Plasmonic Nanostructures Containing Blunt Edges/corners: From Symmetric to Asymmetric Edge Rounding. *ACS Nano* **2012**, *6*, 6492–6506.

(38) Luo, Y.; Lei, D. Y.; Maier, S. A.; Pendry, J. B. Broadband Light Harvesting Nanostructures Robust to Edge Bluntness. *Phys. Rev. Lett.* **2012**, *108*, 023901.

(39) Aubry, A.; Lei, D. Y.; Maier, S. A; Pendry, J. B. Plasmonic Hybridization between

Nanowires and a Metallic Surface : A Transformation Optics Approach. *Nano* **2011**, *5*, 3293–3308.

(40) Giannini, V.; Fernández-Domínguez, A. I.; Sonnefraud, Y.; Roschuk, T.; Fernández-García, R.; Maier, S. A. Controlling Light Localization and Light-Matter Interactions with Nanoplasmonics. *Small* **2010**, *6*, 2498–2507.